Sensors and Materials, Vol. 38, No. 7 (2026) 4069–4084
MYU Tokyo

S & M 4550

Analyses of Stress and Strain in the Optic Nerve of Eyeballs with Different Axial Lengths under G-forces

Chia-Wen Lee,[1,2] Peng-San Cheng,[3] Chao-Ming Hsu,[3]
Jiehui Zheng,[1,2] Linda Yi-Chieh Poon,[4,5*] and Cheng-Fu Yang[6,7**]

[1]Marine Culture & Tourism Integration of Fujian Higher Educational Applied Liberal Arts Research Center, Xiamen 361102, China
[2]School of Information Engineering, Xiamen Ocean Vocational College, Xiamen 361102, China
[3]Department of Mechanical Engineering, National Kaohsiung University of Science and Technology, Kaohsiung 807, Taiwan
[4]Department of Ophthalmology, Kaohsiung Chang Gung Memorial Hospital, Kaohsiung 833, Taiwan
[5]School of Medicine, Chang Gung University, Taoyuan 333, Taiwan
[6]Department of Chemical and Materials Engineering, National University of Kaohsiung, Kaohsiung 811, Taiwan
[7]Department of Aeronautical Engineering, Chaoyang University of Technology, Taichung 413, Taiwan

(Received November 18, 2025; accepted June 30, 2026)

Keywords: stress and strain, optic nerve of eyeballs, different axial lengths, G-forces

In this study, we employed finite element analysis to investigate the biomechanical responses of the optic nerve under varying G-forces and intraocular pressures (IOPs). Six eyeball models were constructed using SolidWorks, including a porcine eye and five human eyes with axial lengths of 22, 24, 26, 28, and 30 mm, corresponding to hyperopia, emmetropia, and varying degrees of myopia. These models were imported into ANSYS for modal and transient dynamic analyses. The modal analysis results indicate that increasing axial length leads to decreases in natural frequencies across all modes, while the mode shapes remain similar regardless of axial variation. In the dynamic G-force simulations, the eyeball was constrained to displace only along the primary loading axis, and G-force was increased incrementally from 1G to 6G. The analysis reveals that beyond 3G, differences in flight posture and IOP have a limited effect on the trends of stress and strain in the optic nerve. However, eyes with higher IOP exhibit greater internal pressure responses during loading than those with lower IOP. These findings suggest that axial elongation significantly alters the mechanical behavior of the eye, reducing structural stiffness, whereas elevated IOP amplifies internal stress distribution. The results provide insight into ocular safety in high-acceleration environments and contribute to understanding biomechanical risk factors for optic nerve damage in individuals with myopia or elevated IOP. The objective of this study is to establish a sensor-assisted biomechanical framework for analyzing ocular responses under varying IOPs and dynamic loading conditions. The present model assumes fixed IOP values and does not consider physiological aqueous humor regulation. Future work will integrate physiological mechanisms and advanced ocular sensing concepts to improve the prediction of ocular behavior under complex loading environments.

*Corresponding author: e-mail: lindap@cgmh.org.tw
**Corresponding author: e-mail: cfyang@nuk.edu.tw
https://doi.org/10.18494/SAM6066

ISSN 0914-4935
https://myukk.org/

1. Introduction

Intraocular pressure (IOP) plays a vital role in maintaining the structural stability and physiological function of the human eye.[1] It is primarily determined by the balance between aqueous humor production and its drainage through the trabecular meshwork and uveoscleral outflow pathways. Abnormal fluctuations in IOP can lead to various ocular disorders, most notably glaucoma, which is one of the leading causes of irreversible blindness worldwide. Elevated IOP increases the mechanical stress on the optic nerve head and surrounding tissues, resulting in the deformation of the lamina cribrosa and the subsequent loss of retinal ganglion cells. Conversely, abnormally low IOP, or ocular hypotony, can compromise the structural integrity of the eyeball, leading to vision distortion and potential retinal detachment. Understanding the biomechanical behavior of the eye under varying IOP levels (IOPs) is therefore essential for elucidating the mechanisms underlying optic nerve damage and for improving diagnostic and therapeutic strategies. Such analysis requires a multidisciplinary approach that combines physiology, material mechanics, and computational modeling to accurately capture the complex stress–strain interactions within ocular tissues.[2]

Over the past decades, a variety of sensor technologies have been developed to measure IOP, ranging from traditional contact tonometry to advanced implantable micro-sensors and optical systems.[3–5] Goldmann applanation tonometry, for instance, has long been considered the clinical standard owing to its simplicity and reliability; however, it provides only static measurements and requires corneal contact, which may affect accuracy. Noncontact tonometers using air-puff techniques offer improved patient comfort but often suffer from limited precision under varying corneal thickness conditions. More recently, MEMS[6] and wireless[7] implantable pressure sensors have been introduced to enable the continuous monitoring of IOP in real time. Despite their promising potential, such devices face challenges including biocompatibility, long-term stability, power supply management, and potential risks of infection or tissue irritation. Additionally, calibration drift over time and individual anatomical variations can lead to measurement errors. Consequently, while sensor-based techniques have significantly advanced the monitoring of ocular pressure, they remain limited in their ability to capture the complex dynamic and biomechanical interactions that occur within the eye under physiological or pathological loading conditions.

To address the limitations of conventional sensor-based methods, in this study, we adopted a computational simulation approach to analyze the effects of IOP on the ocular system. To enhance the biomechanical analysis, an IOP sensing mechanism was integrated into the models. This sensor-based approach allows for the real-time detection of pressure variations within the eyeball during simulations, providing critical data for evaluating stress and strain distributions across ocular structures. Incorporating pressure sensing improves the fidelity of the simulation, enabling the more precise assessment of the biomechanical responses of the optic nerve and other ocular tissues under different loading conditions. By simulating physiological conditions, such as varying IOPs and external mechanical forces, the model can predict localized deformation and stress propagation within ocular tissues. This approach not only eliminates the limitations associated with physical measurements but also offers a safe, cost-effective, and repeatable means of investigating the dynamic behavior of the eye under different clinical or environmental scenarios.

In this study, we employed the finite element method (FEM) to simulate the mechanical response of the human eyeball under different IOPs and axial lengths. The FEM-based model enables a detailed examination of stress, strain, and resonance frequency variations across ocular structures, particularly focusing on the optic nerve and sclera. The analysis encompasses modal and harmonic response simulations to investigate how variations in eyeball geometry affect its dynamic behavior. Comparisons with experimental data from previous studies were used to validate the model, confirming its accuracy in reproducing realistic vibrational patterns and resonance frequencies. Furthermore, we explored the correlation between axial length and the natural frequencies of the eyeball, providing insight into how elongation, which is commonly associated with myopia, affects the biomechanical stability of ocular tissues. The outcomes of this research contribute to a more comprehensive understanding of ocular biomechanics, offering a theoretical foundation for the clinical diagnosis, prevention, and treatment of vision-related diseases induced by abnormal mechanical stress.

Previous studies have primarily focused on IOP measurement, ocular resonance analysis, or biomechanical responses under static loading conditions. Although several finite element (FE) investigations have examined stress distributions in ocular tissues, most studies considered either IOP effects or geometric variations independently and rarely addressed the combined effects of IOP, flight posture, axial length, and dynamic G-force loading. In contrast, we established a unified FE framework capable of evaluating the coupled biomechanical responses of the optic nerve under multiple physiological and environmental conditions. This approach enables a more comprehensive assessment of ocular behavior in high-acceleration environments and provides a foundation for future sensor-assisted ocular monitoring systems.

Rather than focusing solely on the mechanical effects of high-G environments, the objective of this study is to establish a sensor-assisted biomechanical simulation framework for investigating the interactions among IOP, ocular deformation, and dynamic external loading. Existing ocular pressure sensing technologies primarily provide pressure measurements but are unable to directly characterize internal stress and strain distributions within ocular tissues. By integrating FE analysis with pressure-sensing concepts, the proposed framework provides a virtual platform for evaluating biomechanical responses that are difficult to obtain experimentally. The high-G loading scenario was selected as a representative case study because it introduces complex dynamic conditions under which conventional sensing approaches are often insufficient. The results obtained from this framework may serve as a theoretical basis for the future development of intelligent ocular sensing systems, dynamic IOP monitoring devices, and biomechanically informed sensor designs for clinical and aerospace applications.

The biomechanical information obtained from the present simulation framework may also contribute to the development of next-generation ocular sensing technologies. Unlike conventional tonometry systems that primarily provide static IOP measurements, the stress, strain, and pressure distributions predicted in this study identify critical regions of mechanical sensitivity within the optic nerve and surrounding ocular tissues under dynamic loading conditions. These findings may support the design of advanced sensing platforms, including MEMS-based implantable pressure sensors, flexible strain sensors, fiber-optic sensors, and smart contact lens sensors capable of continuously monitoring biomechanical responses in real time. Furthermore, the simulation framework can serve as a virtual testing environment for sensor placement optimization, sensitivity evaluation, and calibration under varying IOPs and acceleration conditions. Such integration of computational biomechanics and sensing technologies may facilitate the development of more accurate and adaptive ocular monitoring systems for aerospace medicine, glaucoma assessment, and high-risk visual health applications.

2. Methodology

All FE simulations were performed using ANSYS Workbench 19.2 (ANSYS Inc., Canonsburg, PA, USA). Physiological differences among individuals lead to variations in eyeball dimensions. In this study, anatomical parameters of ocular components were derived from ophthalmological data and relevant literature.[8,9] The left human eyeball model was constructed in SolidWorks, including the sclera, cornea, ciliary body, suspensory ligaments, optic nerve, aqueous humor, and vitreous body, all enclosed by a circumferential layer of orbital fat. The complete model configuration is shown in Fig. 1, with all parts smoothly integrated without gaps. For a typical human eye, the average axial length is 24 mm, width 22.5 mm, corneal radius 7.6 mm, corneal thickness 5.5 mm, scleral radius 11.25 mm, and scleral thickness 0.75 mm. The lens curvature radii are 10 mm (anterior) and 6 mm (posterior), whereas the optic nerve lies slightly inferior and nasal to the eyeball axis with a maximum diameter of 1.8 mm. Six distinct eyeball models were developed in this study: a porcine eye for comparison with experimental data, and human eyes with axial lengths of 22 mm (hyperopia), 24 mm (normal), 26 mm (myopia, −600 D), 28 mm (myopia, −1200 D), and 30 mm (myopia, −1800 D). The porcine eye was selected for validation purposes because its anatomical structure, ocular dimensions, and biomechanical properties are relatively similar to those of the human eye. In ophthalmic

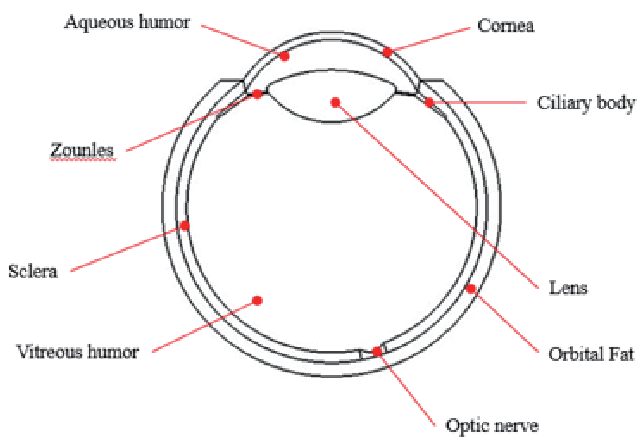

Fig. 1. (Color online) Structural diagram of the eyeball with axial length of 24 mm.

biomechanics research, porcine eyes are widely used as experimental models owing to their availability and their ability to provide representative mechanical responses. Therefore, the porcine eye model was employed to facilitate comparison with previously published experimental data and to support the validation of the proposed FE framework.

The generation of FEM meshes for these models involved two primary stages: geometric construction and element discretization. Once the FE mesh was established, material properties, boundary conditions, and loading parameters were assigned to each element using established mathematical modeling techniques. Accurately representing the material properties of ocular tissues is crucial for obtaining reliable FE simulation results. Given the complex structure of the eyeball, which consists of multiple tissue types and materials, the necessary material parameters were obtained from relevant literature and experimental data. In this study, the ocular tissues were assumed to exhibit isotropic elastic behavior. Within the software library, each component was defined by its Young's modulus, Poisson's ratio, and density, which describe the relationship between stiffness, deformation, and mass distribution. These parameters are summarized as follows.

Cornea: density = 1024 kg/m^3, Poisson's ratio = 0.49, Young's modulus = 0.4 MPa

Sclera: density = 1049 kg/m^3, Poisson's ratio = 0.47, Young's modulus = 3 MPa

Lens: density = 1500 kg/m^3, Poisson's ratio = 0.49, Young's modulus = 1.5 MPa

Ciliary body: density = 1600 kg/m^3, Poisson's ratio = 0.49, Young's modulus = 11 MPa

Suspensory ligaments: density = 1000 kg/m^3, Poisson's ratio = 0.47, Young's modulus = 0.89 MPa

Aqueous humor: density = 999 kg/m^3, Poisson's ratio = 0.49, Young's modulus = 0.037 MPa

Vitreous humor: density = 999 kg/m^3, Poisson's ratio = 0.49, Young's modulus = 0.042 MPa

Optic nerve: density = 1008 kg/m^3, Poisson's ratio = 0.49, Young's modulus = 0.03 MPa

Orbital fat: density = 1000 kg/m^3, Poisson's ratio = 0.48, Young's modulus = 0.00296 MPa

After constructing the eyeball model, the contact surfaces for resonance analysis were defined on the outer sclera using the ANSYS's built-in modeling module. For G-force analysis, contact and boundary surfaces were set at the attachment points of the extraocular muscles, including the superior, inferior, medial, and lateral rectus. Owing to physiological variation, the eyeball mass reported in the literature slightly differs from the simulation values. In this study, the simulation was validated using experimental data from Shih and Guo.(10) The model was built on the basis of literature data, with an average eyeball volume of 6.9 cm^3 and a mass of 6.6 g, whereas the simulated model showed 6.84 cm^3 and 6.9 g, resulting in volume and mass errors of 0.8 and 4.3%, respectively. For transient analysis under G-forces, the simulation examined variations in different flight postures and IOPs. A time step of 0.1 s was used to capture detailed temporal responses, and motion was constrained along the Y-axis to avoid unwanted displacements. The applied G-force increased by 1 G (9.8 m/s^2) per second, reaching a maximum of 6G over a total simulation period of 6 s. Three representative flight conditions were considered in this study: vertical climb, level flight, and vertical fall. These conditions correspond to the upright, horizontal, and inverted body orientations of the eyeball model, respectively. Specifically, the vertical climb condition represents an upright (head-up) orientation, the level-flight condition represents a horizontal orientation, and the vertical-fall condition represents an inverted (head-down) orientation. Although different terms are used to describe the flight condition and body orientation, they refer to the same loading configurations throughout this study.

3. Simulation Results and Discussion

In this study, a mesh convergence analysis was performed using adjusted mesh elements in combination with the remeshing function. Stress variations were extracted at both the apex of the sclera and the optic nerve to evaluate mesh convergence. Figure 2 illustrates the extraction point at the scleral apex [Fig. 2(a)] and the results of the convergence analysis [Fig. 2(b)]. As shown in Fig. 2(b), the stress values at both the sclera and the optic nerve stabilized when the mesh consisted of 375000 elements, with numerical errors within 1%. On the basis of these results, a mesh of 375000 elements was adopted for subsequent analyses. The convergence analysis confirms that the selected mesh density is sufficient to produce accurate and reliable stress predictions while minimizing computational cost. This approach ensures that the FM model can capture localized stress concentrations in the sclera and optic nerve without introducing significant numerical artifacts, thereby improving the robustness and credibility of the biomechanical simulations.

In this section, we analyze the effects of G-force on the stress, strain, and pressure exerted on the optic nerve in eyes with normal axial length under different IOPs. The optic nerve responses were evaluated, and surface pressure was calculated using P = F/A with an effective contact area of 0.17 mm^2. Figures 3 and 4 show the variations in optic nerve stress and strain under three flight postures and IOPs from 10 to 50 mmHg as G-force increases. The results indicate that, regardless of posture, stress and strain exhibit similar trends across IOPs, increasing progressively with G-force. Higher IOP slightly raises the baseline stress and strain, but the rate of change remains nearly constant. This suggests that the mechanical loading imposed by

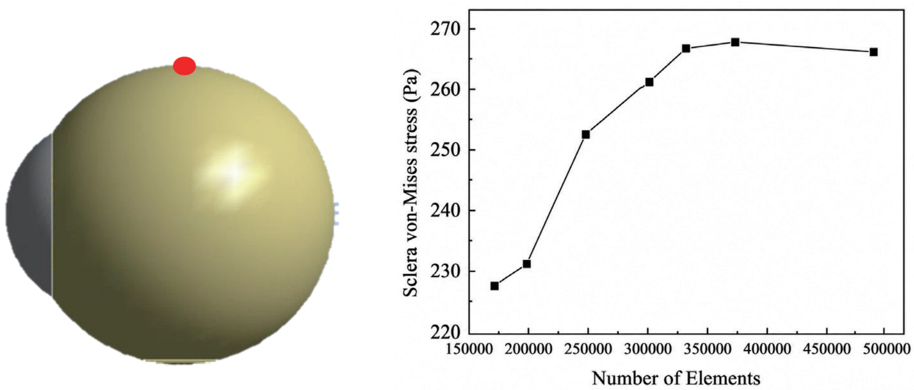

(a) (b)

Fig. 2. (Color online) (a) Scleral data extraction location and (b) results of convergence analysis of element quantity in the FE model.

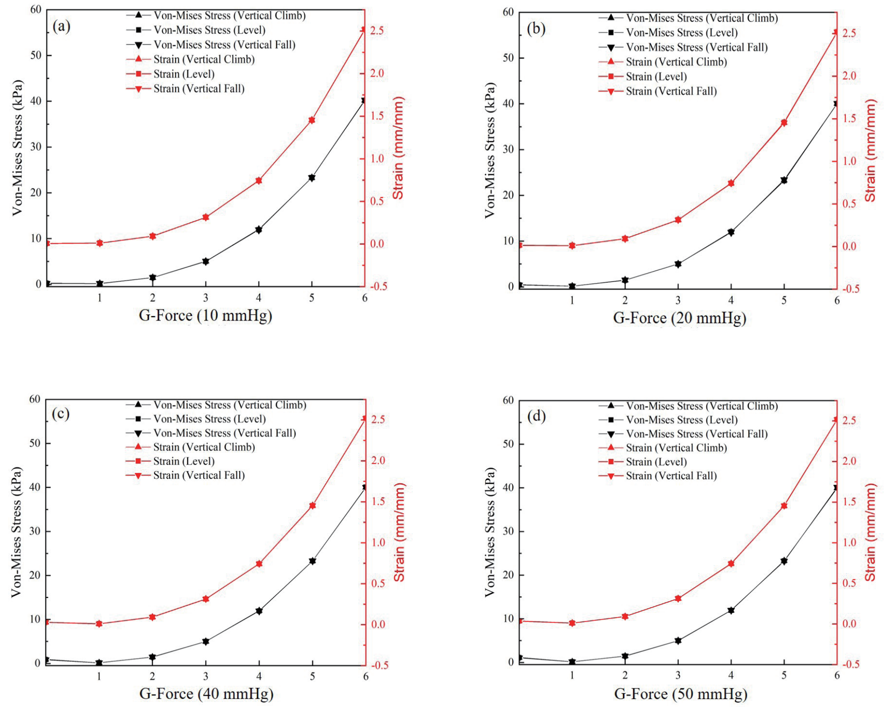

Fig. 3. (Color online) Variation trends of optic nerve stress and strain under three flight postures at different IOPs, namely, (a) 10, (b) 20, (c) 40, and (d) 50 mmHg, as G-force increases.

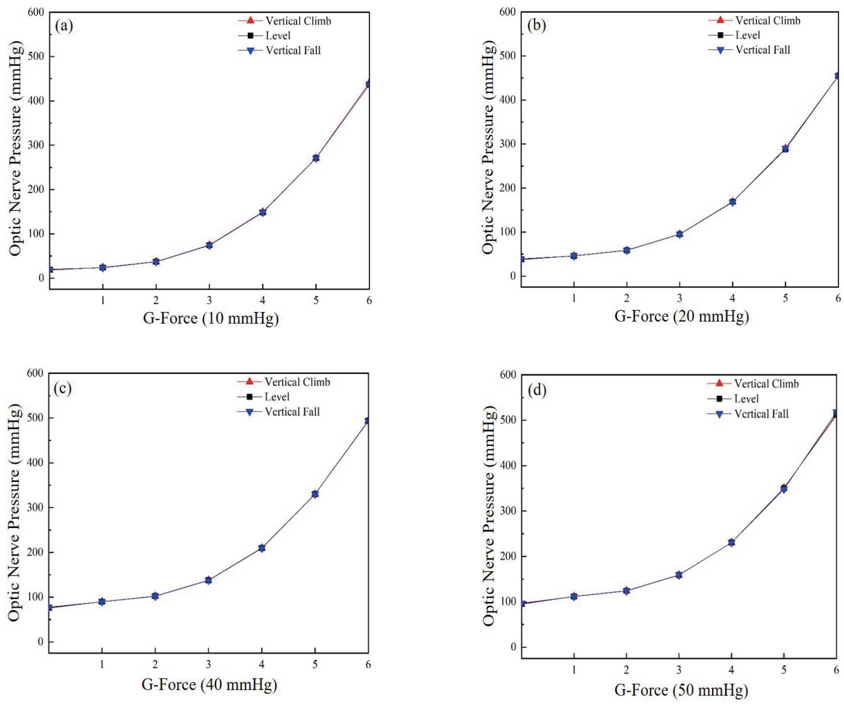

Fig. 4. (Color online) Variation trends of optic nerve pressure under three flight postures at different IOPs, namely, (a) 10, (b) 20, (c) 40, and (d) 50 mmHg, as G-force increases.

G-force plays a dominant role in optic nerve deformation, while IOP contributes as a secondary factor. These results suggest that G-force is the dominant mechanical factor affecting optic nerve deformation, with IOP acting as a secondary modulating parameter. This has important implications for high-G environments such as military aviation, aerospace missions, and high-performance aircraft operations. Prolonged or repeated exposure to high G-forces may induce mechanical strain that can contribute to optic nerve head deformation, potentially increasing the risk of visual disturbances or long-term ocular damage. Therefore, understanding the interplay between IOP and acceleration loading may assist in developing protective measures, flight safety protocols, and training guidelines to mitigate ocular risks for aircrew members and astronauts.

Figure 5 presents the stress and strain responses of the optic nerve under five IOPs across three body orientations at different G-force levels. Figure 5(a) represents the baseline condition before acceleration; the trends of optic nerve stress and strain consistently follow the order: upright > horizontal > inverted. Additionally, both stress and strain increase with increasing IOP, indicating that elevated IOP contributes to greater mechanical loading on the optic nerve in the absence of external acceleration. However, the behavior changes once acceleration begins. Figure 5(b), corresponding to 1G acceleration, shows that the trends among the three postures become less regular, and the effect of IOP begins to reverse. The results obtained at 2G acceleration were highly similar to those at 1G; therefore, they are not presented separately here. At these stages, increasing IOP results in lower stress and strain magnitudes. This phenomenon suggests that under external acceleration, higher IOP may act to stiffen the ocular structure, redistributing load away from the optic nerve head and partially mitigating deformation.

As shown in Figs. 5(c) (3G) and 5(d) (5G), the optic nerve stress and strain values obtained under the three flight postures and five IOP conditions become highly similar. The curves remain nearly constant with only minor fluctuations, indicating that the differences among postures and IOP levels are considerably reduced at higher acceleration levels. These results suggest that the mechanical response of the optic nerve converges as G-force increases, with external inertial loading becoming the dominant factor governing tissue deformation. This indicates that at sufficiently high acceleration, the external inertial force dominates the mechanical response, overpowering the effects of both posture and IOP. Consequently, the optic nerve experiences similar levels of mechanical strain regardless of physiological eye pressure or body orientation once the G-load reaches 3G. These findings highlight a transition in mechanical sensitivity:

At low or no acceleration, IOP is the primary factor affecting optic nerve stress and strain.

At moderate acceleration, both posture and IOP interact in a nonlinear manner.

At high acceleration (≥3G), G-force becomes the dominant determinant, and the effects of posture and IOP are significantly diminished.

This suggests that in high-G environments, such as fighter aviation and spaceflight operations, structural loading on the optic nerve is largely unavoidable, and protective strategies should focus on limiting prolonged exposure to high G-forces, improving anti-G suit

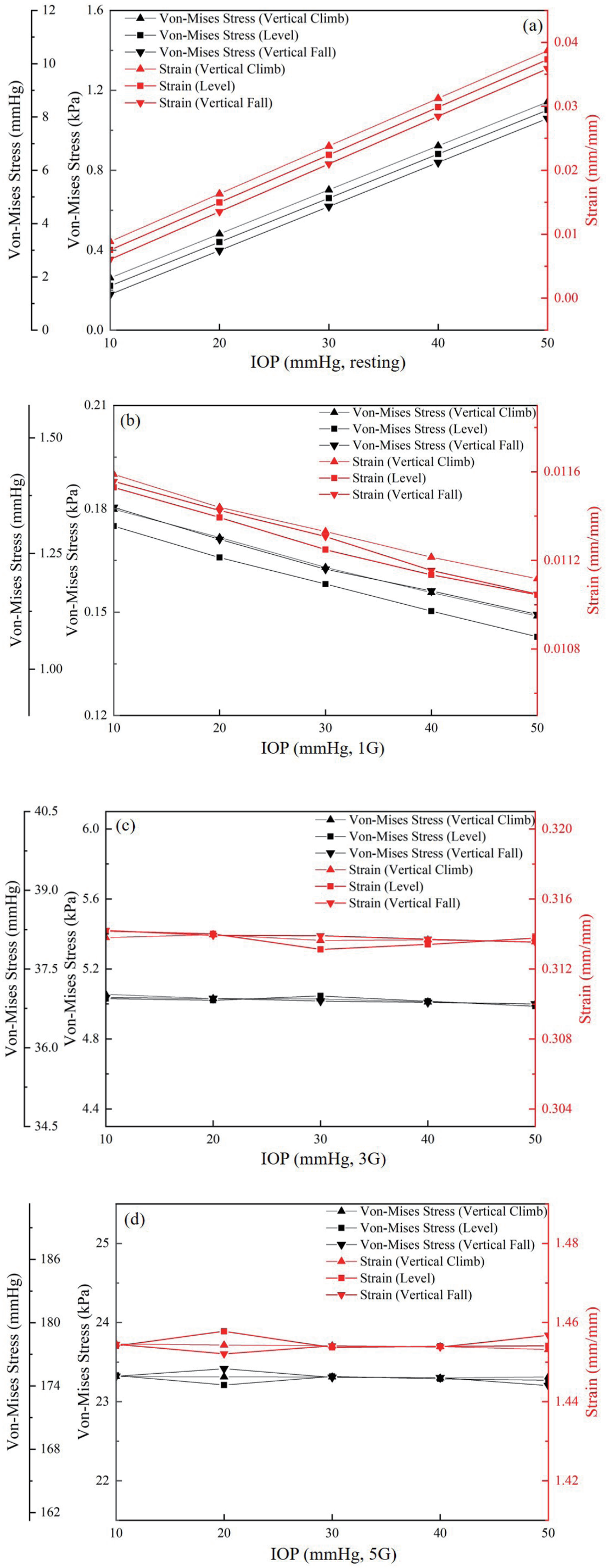

Fig. 5. (Color online) Analysis results of optic nerve stress and strain under three flight postures at various IOPs and G-forces: (a) resting and during acceleration to (b) 1G, (c) 3G, and (d) 5G.

effectiveness, and considering ocular health evaluations for personnel with pre-existing elevated IOP or glaucoma risk.

Figure 6 presents the optic nerve pressure distribution under varying G-forces for three flight postures across five IOP conditions. From Figs. 6(a) to 6(g), it can be observed that, at a given IOP, the pressure exerted on the optic nerve remains relatively similar among the three postures, indicating that posture alone has a limited direct effect on optic nerve loading within the examined acceleration range. However, both increasing G-force and increasing IOP consistently lead to a progressive rise in optic nerve pressure. As the G-force increases, the inertial load transmitted through the ocular tissues becomes more pronounced, resulting in greater compressive stress at the optic nerve head. Similarly, a higher IOP elevates the baseline internal pressure within the globe, thereby increasing the initial stress environment before the external acceleration load is applied. The combined effect of G-force and IOP suggests that the optic nerve is subjected to both a dynamic external load and a static internal load, and the interaction of these two effects determines the magnitude of the mechanical stress experienced by the tissue. Consequently, eyes with elevated IOP, such as those in individuals with ocular hypertension or early-stage glaucoma, may exhibit heightened susceptibility to mechanical strain during high-acceleration environments. This outcome highlights the need to consider ocular physiological conditions when assessing tolerance to high-G exposure, particularly in aviation, aerospace, and high-speed maneuver contexts. The findings also imply that protective measures or operational guidelines may be necessary for individuals with higher baseline IOP to reduce the risk of optic nerve deformation or potential damage under sustained G-force loading.

Figures 7 and 8 illustrate the optic nerve stress and strain responses under varying G-forces across five IOP conditions and three flight postures. Prior to acceleration, both stress and strain increase monotonically with IOP, indicating that a higher baseline ocular pressure contributes to a stiffer mechanical environment and greater load on the optic nerve. However, once the acceleration reaches 1G, the relative ordering reverses, and eyes with lower IOP exhibit greater stress and strain than those with higher IOP. This inversion suggests that, under dynamic loading, low-IOP eyes may undergo greater deformation due to reduced structural resistance, whereas high-IOP eyes maintain their shape more effectively. As the acceleration increases further, reaching 3G, the effects of posture and IOP on stress and strain become less distinct, and the differences among conditions diminish. Despite this convergence, the overall magnitude of stress and strain continues to increase with G-force, demonstrating that inertial loading becomes the dominant mechanical factor at higher accelerations. These results further support this observation through optic nerve pressure analysis, which shows a minimal variation among different postures at a given IOP, but consistent increases in pressure as IOP increases.

Under varying G-forces, the pressure hierarchy remains positively correlated with IOP, indicating that baseline globe pressure continues to contribute to optic nerve loading even when G-force becomes the major driving factor. These results also highlight a nonlinear mechanical interaction between static internal pressure and dynamic acceleration forces. At low acceleration levels, ocular rigidity driven by IOP plays a significant role in shaping optic nerve biomechanics, but at high acceleration levels, inertial forces begin to overwhelm these baseline structural

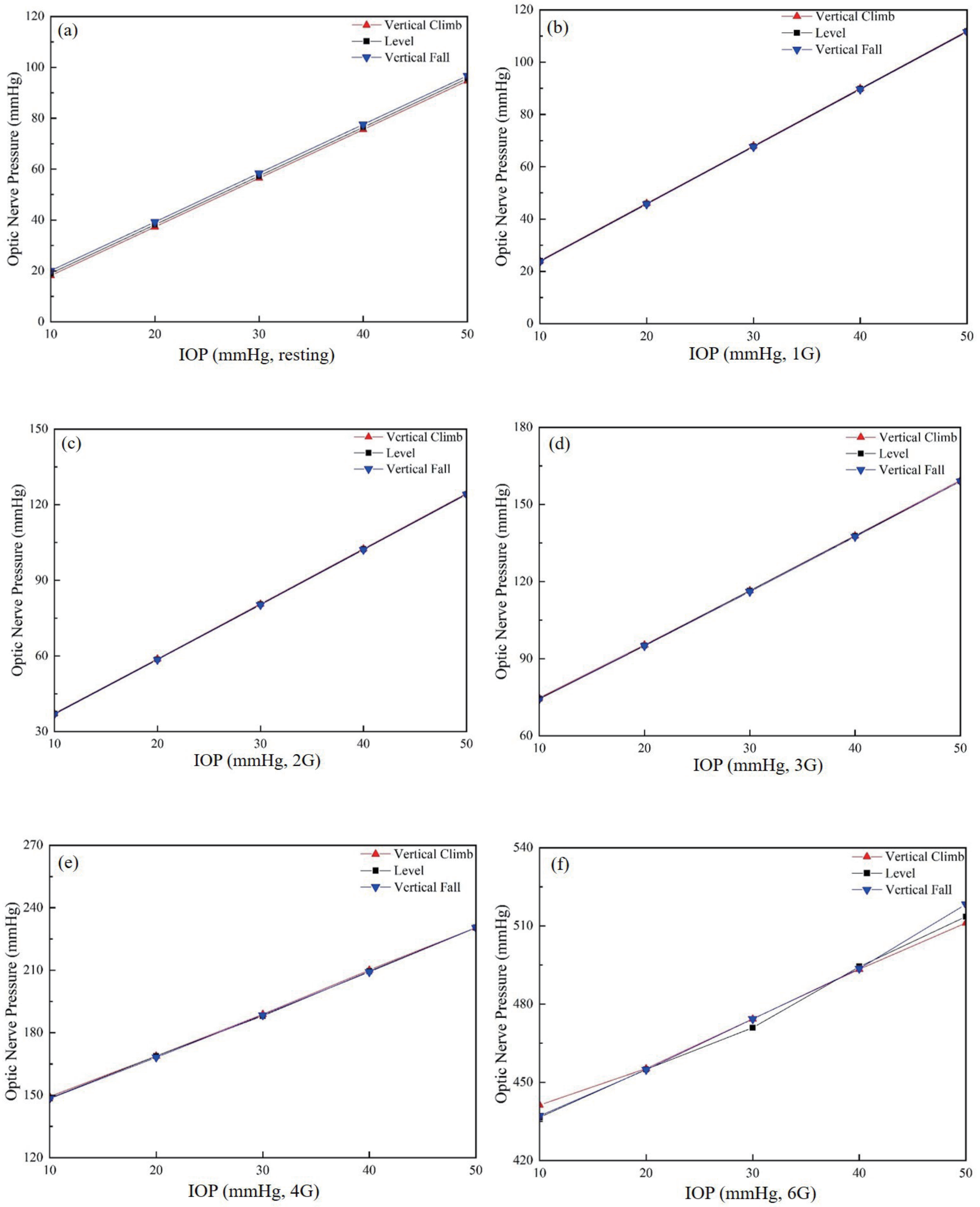

Fig. 6. (Color online) Variation trends of optic nerve pressure under three flight postures at different IOPs and G-forces: (a) resting and during acceleration to (b) 1G, (c) 2G, (d) 3G, (e) 4G, and (f) 6G.

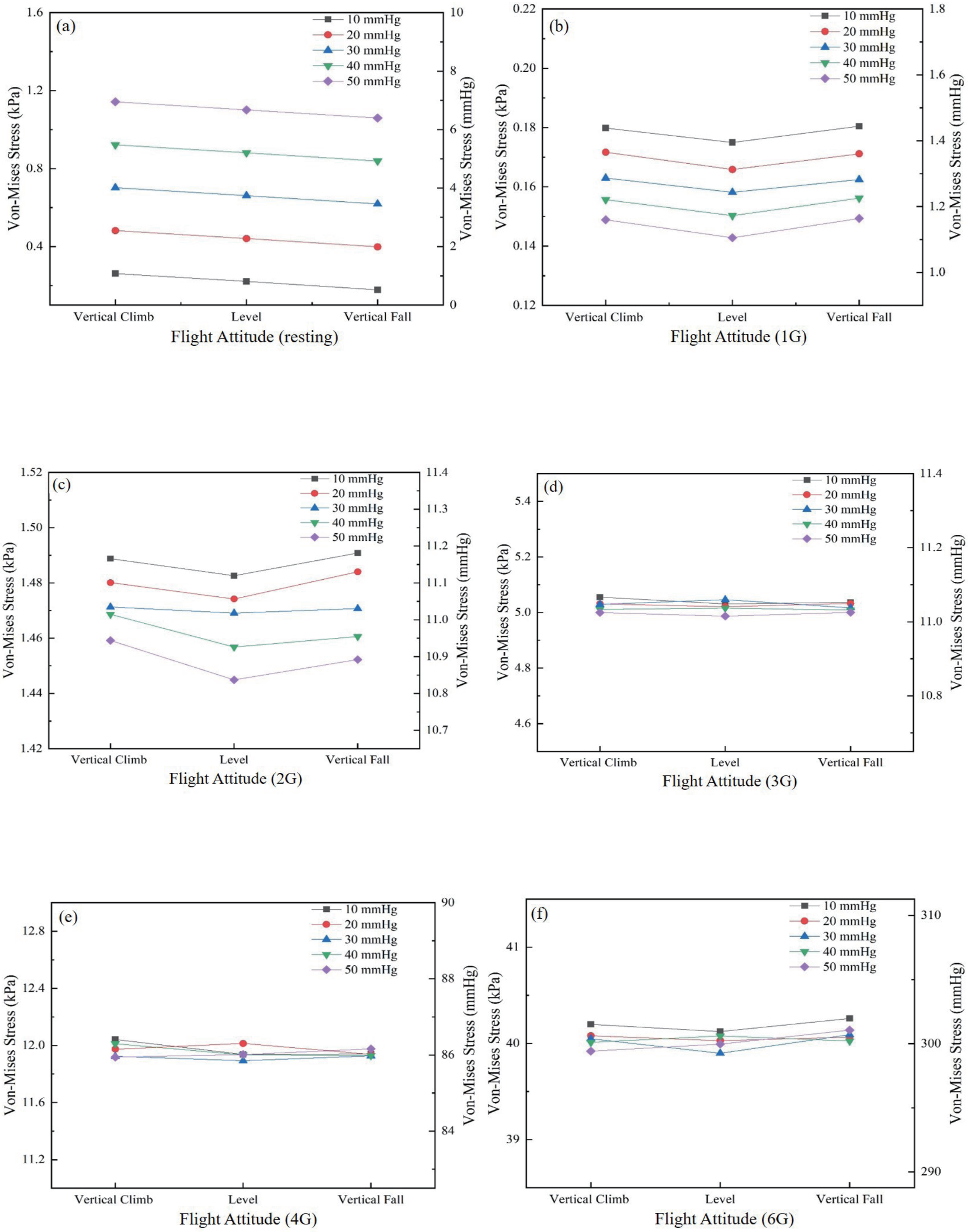

Fig. 7. (Color online) Analysis results of optic nerve stress under five IOPs across three flight postures at different G-forces: (a) resting and during acceleration to (b) 1G, (c) 2G, (d) 3G, (e) 4G, and (f) 6G.

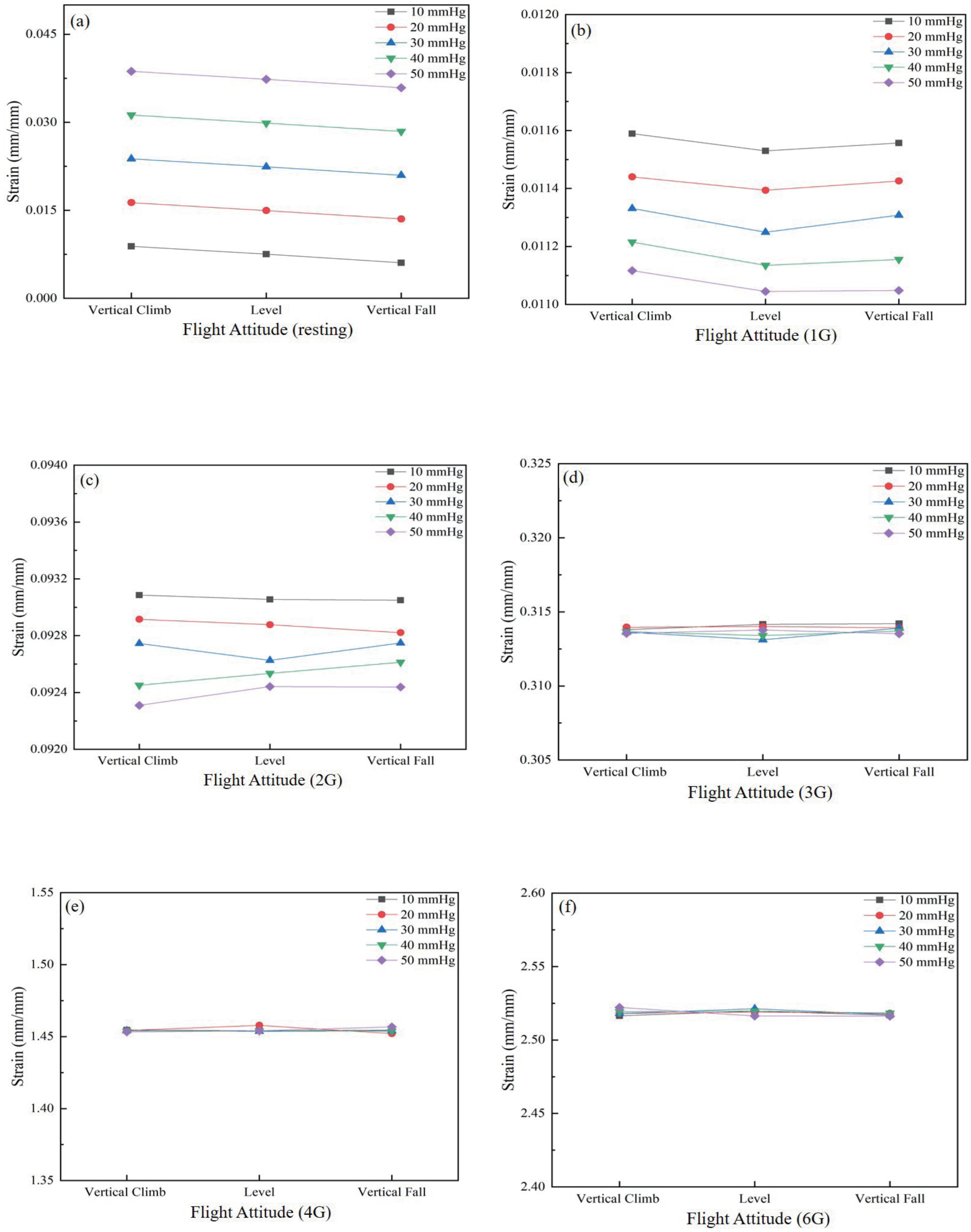

Fig. 8. (Color online) Optic nerve strain analysis results under five IOPs across three flight postures at different G-forces: (a) resting and during acceleration to (b) 1G, (c) 2G, (d) 3G, (e) 4G, and (f) 6G.

differences. This finding has practical implications for aviation and aerospace physiology. Individuals with elevated IOP may be at increased risk of sustained optic nerve pressure under high-G conditions, whereas individuals with low IOP may be more susceptible to deformation-related strain during initial acceleration. Understanding this balance is critical for developing operational guidelines, protective strategies, and potential screening recommendations for pilots, astronauts, and high-performance aircraft personnel.

Note that the present simulations were conducted under prescribed IOP conditions, and the dynamic physiological regulation of aqueous humor was not included in the model. In reality, exposure to high-G environments may alter aqueous humor production, drainage efficiency, episcleral venous pressure, and ocular blood flow, potentially resulting in time-dependent changes in IOP. These physiological responses can interact with the mechanical effects of acceleration and further affect stress and strain distributions within ocular tissues. Therefore, the current model primarily represents the biomechanical response of the eye under fixed IOP conditions. Future studies may incorporate fluid–structure interaction models and physiological regulation mechanisms to investigate the coupled effects of aqueous humor dynamics and mechanical loading under high-acceleration environments.

The present study is based on a FE simulation framework and does not directly reproduce all physiological responses occurring in real-world high-G environments. The model was constructed using the anatomical and biomechanical data reported in the literature and validated through comparison with previously published experimental observations. Consequently, the simulations provide a realistic approximation of ocular biomechanical behavior under controlled loading conditions. Nevertheless, actual physiological responses may be affected by additional factors, including aqueous humor dynamics, ocular blood flow regulation, individual anatomical variability, and adaptive responses to acceleration exposure. Future studies will incorporate these physiological mechanisms and compare simulation results with experimental and clinical measurements to further improve model accuracy and real-world applicability. The proposed framework may also serve as a virtual testing platform for evaluating future ocular sensing technologies and validating sensor performance under dynamic loading conditions that are difficult to investigate experimentally.

4. Conclusions

A particularly novel finding of this study is the identification of a transition in the dominant biomechanical factor governing optic nerve responses. The results indicate that IOP plays a major role under resting and low-acceleration conditions, whereas the effects of posture and IOP become progressively weaker as acceleration increases. When the G-force exceeds approximately 3G, the mechanical response of the optic nerve is dominated primarily by inertial loading, resulting in similar stress and strain levels across different postures and IOP conditions. We employed FE analysis to investigate the mechanical responses of the optic nerve in eyes with different IOPs under varying G-force conditions and flight postures. The results demonstrate that both IOP and G-force significantly affect optic nerve stress, strain, and pressure, although their relative effects vary with acceleration magnitude. Before acceleration, eyes with higher IOP exhibited greater stress and strain due to increased internal stiffness. However, at low acceleration levels (e.g., 1G), this relationship reversed, with low-IOP eyes experiencing greater deformation, suggesting that reduced internal support allows greater mechanical displacement under dynamic loading. As G-force increased to 3G and beyond, the effects of posture and IOP became less pronounced, and the optic nerve responses were dominated primarily by inertial forces, leading to a convergence of mechanical behavior across conditions. Nevertheless, pressure at the optic nerve head consistently increased with elevated IOP regardless of posture or G-force, indicating that static internal loading remains a contributing factor even under high acceleration. These findings highlight a nonlinear interaction between internal ocular pressure and external acceleration. Eyes with elevated IOP may be at greater risk of chronic mechanical loading, whereas eyes with low IOP may be more vulnerable to deformation-induced strain during rapid acceleration changes. The results provide valuable insight for aerospace medicine, pilot health assessment, and safety protocols in high-acceleration environments, underscoring the importance of considering individual ocular biomechanics when evaluating tolerance to high-G exposure. Despite the valuable findings obtained in this study, several limitations should be acknowledged. The simulations were performed under prescribed IOP conditions and did not consider dynamic physiological processes such as aqueous humor regulation and ocular blood flow. In addition, ocular tissues were assumed to be homogeneous, isotropic, and linearly elastic. Consequently, the present results represent the fundamental biomechanical responses of the eye under simplified conditions. Accurately characterizing the interactions among IOP, physiological regulation, tissue properties, and external acceleration remains a challenge in ocular biomechanics. Future studies will incorporate physiological regulation mechanisms, fluid–structure interaction analysis, subject-specific material properties, and experimental or clinical validation. Advanced ocular sensing technologies will also be explored to improve the prediction and monitoring of ocular responses under dynamic loading conditions. The proposed framework may further serve as a virtual testing platform for evaluating and optimizing future ocular sensing systems in environments that are difficult to investigate experimentally.

Acknowledgments

This research was supported by projects under Nos. NSTC 113-2622-E-390-001 and NSTC 113-2221-E-390-011.

References

1 K. Y. Wu, M. Mina, M. Carbonneau, M. Marchand, and S. D. Tran: Micromachines **14** (2023) 1915.
2 S. Chinnaswamy, V. Natarajan, S. Samiappan, and R. Gurumurthy: Eng. Proc. **59** (2023) 179.
3 K. Gillmann, G. E. Bravetti, L. J. Niegowski, and K. Mansouri: Expert Rev. Ophthalmol. **14** (2019) 263.
4 F. D. Silva and M. Lira: Surv. Ophthalmol. **67** (2022) 1319.
5 T. Liu, Y. L. Cai, M. Y. Hu, Z. Wang, X. Liu, M. Chen, and K. Wang: Adv. Ophthalmol. Pract. Res. **5** (2025) 142.

6 P. Zolfaghari, A. D. Yalcinkaya, and O. Ferhanoglu: IEEE Photon. Technol. Lett. **35** (2023) 887.

7 A. Agarwal, A. Shapero, D. Rodger, M. Humayun, Y. C. Tai, and A. Emami: 2018 IEEE Custom Integrated Circuits Conf. (CICC, 08–11 April 2018, San Diego, CA, USA).

8 H. A. Quigley, A. E. Brown, J. D. Morrison, and S. M. Drance: Arch. Ophthalmol. **108** (1990) 51.

9 I. A. Sigal, J. Grimm, J. S. Schuman, L. Kagemann, H. Ishikawa, and G. Wollstein: IEEE Trans. Med. Imaging **33** (2014) 1381.

10 P.-J. Shih and Y.-R. Guo: J. Acoust. Soc. Am. **139** (2016) 1784.